Department
of
APPLIED MATHEMATICS

Gravity currents at Ormen Lange

by

Frode Vikebø[1], Jarle Berntsen[1] and Gunnar Furnes[2]

Report no. 163 December 2001

UNIVERSITY OF BERGEN
Bergen, Norway

Department of Mathematics
University of Bergen
5008 Bergen
Norway

ISSN 0084-778X

Gravity currents at Ormen Lange

by

Frode Vikebø[1], Jarle Berntsen[1] and Gunnar Furnes[2]

[1]*Mathematical Institute, University of Bergen.*
[2]*Norsk Hydro, Research Center, Sandsli, Norway.*

Report no. 163

December 2001

Gravity currents at Ormen Lange

Frode Vikebø[1], Jarle Berntsen[1] and Gunnar Furnes[2]

[1] *Department of Mathematics , University of Bergen, Norway.*
[2] *Norsk Hydro, Research Center, Sandsli, Norway.*

December 18, 2001

Abstract

Time series of temperature and velocities at Ormen Lange, located in the Storegga region off mid-Norway, indicate that close to the seabed, at depths ranging from 500-1000 m, large temperature fluctuations are accompanied by short peak values in speed. The extreme events are driven by strong pressure gradients, due to strong atmospheric low pressures and/or internal pressure fronts between warmer Atlantic Water (AW) and colder Norwegian Sea Water (NSW). Along the shelf slope at OL we may get steepening of the iso surfaces of density, separating AW and NSW, due to strong Ekman veering during storms or approaching internal density fronts. During such events the density surfaces tend to undershoot their equilibrium level, and as the forcing weakens, the suppressed water may run up along the shelf slope. In this run up phase, peak values in the velocities are often found.

As a result of the run up phase, heavy water may be elevated onto the shelf. Subsequently dense fluid will spread under the influence of forces produced by its own buoyancy and motions of this form are often referred to as gravity currents. They are characterised by the distinctive nature of the front, which consists of a raised head leading a shallower flow behind. The shape of the head and body of the gravity current, along with velocity, depend on a range of parameters. This report investigates the velocities that may occur with parameters of relevance for Ormen Lange.

1 Introduction

Time series of temperature and velocities at Ormen Lange, located in the Storegga region off mid-Norway, indicate that close to the seabed, at depths ranging down to at least 800 m, large temperature fluctuations are accompanied by a short peak value in speed. Ormen Lange is in the core of the Storegga slide and is currently being considered for development under the leadership of Norsk Hydro. Exploiting the gas reservoir involves seabed pipeline tracks, which makes it essential to know the maximum velocities in the region and to investigate the possibility of forecasting them. Earlier reports have focused on the connection between atmospheric forcing and the occurrence of the above mentioned events (Eliassen et al. (2000), Vikebø et al. (2001a), Vikebø et al (2001b). and Mathisen, Hackett & Engerdahl (2000)) while others have studied the local dynamics using ocean models (Eliassen & Berntsen (2000) and Engedahl & Røed (1999)). Eliassen et al. (2000) present some figures showing how heavy water from depths beyond the shelf edge may be elevated onto the shelf as a result of passing storms. If dense water is transported up on the shelf, it will propagate along the shelf along with Atlantic Water (AW). As the cross shelf oscillations causing the run up retreat, the heavy water on the shelf may be disconnected from the water masses with the same properties, forming a parcel of denser water on the shelf. Owing to gravity these heavy water masses later on flow down valleys or ravines, forced by gravity and pushed by AW, until they reach water with the same density. Vikebø et al. (2001a) present a plausible explanatory model of events, where run up of heavy water is a natural part.

This report will investigate gravity currents flowing down an idealised shelf slope, with sensitivity tests concerning 1) the number of vertical σ-layers, 2) non-hydrostatic physics, 3) initial velocity off shelf, 4) shelf edge profile, 5) slope factor and 6) drag coefficient. In many numerical ocean models, the hydrostatic approximation is made. This approximation causes a considerable saving in computation time. However, if one wants to increase the grid resolution and resolve phenomena on small scale, as for gravity currents, the approximation becomes questionable.

Heggelund & Berntsen (2001) give a description of how to extend the Bergen Ocean Model (BOM) (Berntsen 2000), a σ-coordinate, free surface, C-grid model, to include non-hydrostatic dynamics through a velocity correction term. The report was also a first attempt to investigate possible gravity currents at Ormen Lange. Numerical simulations of gravity currents with the basic equations, with and without the hydrostatic assumption, were made. This report is based on the report by Heggelund & Berntsen (2001).

Section 2 presents review of some theory of relevance. Section 3 consists

of a brief overview of BOM, while Section 4 describes the model setup. In section 5 results are discussed and finally in section 6 the paper is concluded with a short summary and final remarks.

2 Review of relevant theory

When dense fluid is released into a less dense ambient fluid, the dense fluid will spread under the influence of forces produced by its own buoyancy, with a distinct raised head followed by a shallower flow behind. Motion of this form is often referred to as gravity current, and have been studied over a number of years. It has been realized that when the current flows along a horizontal boundary, the head is a controlling feature of the flow. Britter & Simpson (1978) and Simpson & Britter (1979) have shown how the mixing, which occurs immediately behind the head, determinates the rate of advance of the current.

According to Simpson (1987) the motion of a gravity current down a slope is appreciably different from that along a horizontal surface. Britter & Linden (1980) say that for gravity currents flowing down an incline there can be balance between the gravitational force and the frictional and entrainment drag. As a consequence the flow is steady. On the other hand, for horizontal current the frictional and entrainment drag will inevitably decrease the current velocity.

Ellison & Turner (1959) investigated 'Turbulent entrainment in stratified flows' concerning the motion of a dense current down a slope, showing that for the continuous current well behind the head, the mean velocity down the slope was independent of the downstream distance from the source. The thickness of the current, however, increased downstream due to entrainment, maintaining a constant buoyancy flux down the slope. Britter & Linden (1980) investigated 'The motion of the front of a gravity current travelling down an incline' in unstratified water, investigated the possibility that the front of the current, as it is intimately connected to the following flow, is likewise constant downstream the slope. Dimensional analysis shows that the properties of the head are related to the flow variables as follows:

$$\text{Velocity of advance}: \quad U_f = (g_0' Q)^{\frac{1}{3}} f_1(\theta, Re) \tag{1}$$

$$\text{Heigth}: \quad \frac{dH}{dx} = f_2(\theta, Re) \tag{2}$$

$$\text{Length}: \quad \frac{dL}{dx} = f_3(\theta, Re) \tag{3}$$

Average negative buoyancy of the head:

$$\frac{dg_H'}{dx} = (g_0' Q)^{\frac{2}{3}} x^{-2} f_4(\theta, Re) \tag{4}$$

where Q is the volume flow rate per unit width, $g_0' = g(\rho_2 - \rho_1)/(\rho_2 + \rho_1)$, g the gravity, ρ_1 the density of the lighter ambient water, ρ_2 the density of the

dense water, θ the angle of the slope, $Re = (g_0'Q)^{\frac{1}{3}}H/\nu$ is a Reynolds number of the flow, ν the kinematic viscosity of the fluid and H and L the height and length of the head. The x-axis points in the downstream direction. (Britter & Linden 1980) restricted their attention to the case where the Reynolds number was large enough so that the functions $f_i (i = 1, \ldots, 4)$ were functions of slope factor only.

The experimental results of (Britter & Linden 1980) showed that

- For very small slopes ($\theta_c \leq 0.5°$) the head decelerates with distance from the source. At greater slopes the buoyancy force is large enough to overcome frictional effects and a steady head velocity results.

- For a Boussinesq plume the front velocity is found to be approximately 60% of the mean velocity of the following flow. This means that the head increases in size as it travels down the slope, both by direct entrainment into the head itself and by addition of fluid from the following flow. Direct entrainment increases with increasing slope and accounts for one-tenth of the growth of the head at 10° and about two-thirds at 90°.

- The velocity of the front show small variations with θ. Gravitational force increases with slope, but so also does entrainment, both into the head itself and the flow behind. This produces an increased retarding force on the current as momentum is imparted to the entrained fluid.

Britter & Linden (1980) conclude that the experimental results agree well with the dimensional analysis presented earlier in this paper, indicating that the motion of the front is determined by the following flow. As a consequence it is possible to match the front onto the following flow and the resulting equation is;

$$\frac{U_f}{(g_0'Q)^{\frac{1}{3}}} = S_2^{\frac{1}{3}} \left(\frac{cos\theta}{\alpha} + \frac{\alpha sin\theta}{2(E + C_D)} \right) \left(\frac{sin\theta}{E + C_D} \right)^{-\frac{2}{3}}, \tag{5}$$

where S_2 is a profile constant $\simeq 0.75$, α is the proportional constant between the streamline velocity and the velocity of the following flow $\simeq 1.2$, E is the entrainment typically $10^{-3}\theta$ and C_D is the drag coefficient due to stress at the lower boundary typically less then 0.02.

When stratification is introduced, both the front and the flow behind the head will inevitably slow down as they reach the level of equal density. However, the theory presented here can be used to estimate plausible velocities at the shelf slope of Ormen Lange close to the shelf edge by introducing

parameters of relevance. Assuming an average (vertically) volume flow rate per unit width off the shelf edge $Q \sim 7\,\mathrm{m^2\,s^{-1}}$ (with peak $Q \sim 20\,\mathrm{m^2\,s^{-1}}$ in the core), reduced gravity $g_0' \sim 0.01\,\mathrm{ms^{-2}}$, slope factor $\theta \sim 1.7°$ and drag coefficient $C_D \sim 0.0025$ (non-dimensional), the velocity of the head will be about $0.5\,\mathrm{ms^{-1}}$ (and $0.6\,\mathrm{ms^{-1}}$ in the core).

3 Bergen Ocean Model

3.1 Introduction

Bergen Ocean Model (BOM) is a three dimensional, free surface, C-grid, time-split σ-coordinate numerical ocean model, with a 2 1/2 level Mellor and Yamada (Mellor & Yamada 1982) turbulence closure scheme. The model was developed at the Institute of Marine Research and the University of Bergen, Department of Mathematics. Documentation of the model is presented in Berntsen (2000). Section 3.2 gives an overview of the basic equations, parametrisation of subgrid scale processes and boundary conditions. Transformation of z- to σ-coordinates is described in Section 3.3. The time integration is split into a two dimensional external mode and a three dimensional internal mode to limit computational cost, Section 3.4. Finally, numerical interpretation of the governing equations and essential BOM routines are described in Section 3.5 and 3.6 respectively. Symbols used in the description of the model are presented in Appendix A.

3.2 The basic equations

The basic equations of the BOM model are the Reynolds momentum equations with the Boussinesq approximation, (density differences are neglected unless multiplied by gravity). Presented in cartesian coordinates x, y and z, they are as follows:

$$\frac{\partial U}{\partial t} + \vec{U} \cdot \nabla U + W\frac{\partial U}{\partial z} - fV = -\frac{1}{\rho_0}\frac{\partial p}{\partial x} + F_x \quad , \tag{6}$$

$$\frac{\partial V}{\partial t} + \vec{U} \cdot \nabla V + W\frac{\partial V}{\partial z} + fU = -\frac{1}{\rho_0}\frac{\partial p}{\partial y} + F_y \quad , \tag{7}$$

$$\frac{\partial W}{\partial t} + \vec{U} \cdot \nabla W + W\frac{\partial W}{\partial z} = -\frac{1}{\rho_0}\frac{\partial p}{\partial z} - \frac{\rho g}{\rho_0} + F_z \quad , \tag{8}$$

where F_x, F_y and F_z are the viscosity/eddy-viscosity terms.

If the hydrostatic approximation is made (the height of the fluid identically balances the downward pressure) the third equation becomes:

$$\frac{\partial p}{\partial z} = -\rho g \tag{9}$$

The Boussinesq and the hydrostatic approximation are valid as long as the horizontal scale is large compared with the vertical scale and if the density differences are small. Using the above assumptions, the shallow water equations are derived. The equation of continuity, assuming incompressibility,

is

$$\frac{\partial U}{\partial x} + \frac{\partial V}{\partial y} + \frac{\partial W}{\partial z} = 0 \quad . \tag{10}$$

Integrating equation 9 vertically gives the pressure at depth z;

$$P = P_{atm} + g\rho_0\eta + g\int_z^0 \rho(\acute{z})d\acute{z} \quad . \tag{11}$$

The conservation equations for temperature and salinity are

$$\frac{\partial T}{\partial t} + \vec{U}\cdot\nabla V + W\frac{\partial T}{\partial z} = \frac{\partial}{\partial z}\left(K_H\frac{\partial T}{\partial z}\right) + F_T \quad , \tag{12}$$

and

$$\frac{\partial S}{\partial t} + \vec{U}\cdot\nabla S + W\frac{\partial S}{\partial z} = \frac{\partial}{\partial z}\left(K_H\frac{\partial S}{\partial z}\right) + F_T \quad . \tag{13}$$

The density field is computed according to the equation of state,

$$\rho = \rho(S,T,P) \quad , \tag{14}$$

defined by UNESCO (Gill 1982), in the form presented by Wang (1984):

$$\rho = \rho(S,T) \quad . \tag{15}$$

Motions and diffusive losses induced by small scale processes (sub-grid scale) are parameterised by horizontal and vertical eddy viscosity/diffusivity terms. The horizontal terms F_x and F_y in equation (1) and (2) respectively, are given as

$$F_{x,y} = \frac{\partial}{\partial x}\left(A_M\frac{\partial(U,V)}{\partial x}\right) + \frac{\partial}{\partial y}\left(A_M\frac{\partial(U,V)}{\partial y}\right) \quad . \tag{16}$$

The horizontal terms F_T and F_S in equation 12 and 13 are given as

$$F_{T,S} = \frac{\partial}{\partial x}\left(A_H\frac{\partial T,S}{\partial x}\right) + \frac{\partial}{\partial y}\left(A_H\frac{\partial T,S}{\partial y}\right) \quad , \tag{17}$$

similar to the horizontal eddy viscosity terms in equations (1) and (2). The horizontal viscosity and diffusivities, A_M and A_H, may be computed according to (Smagorinsky 1963)

$$(A_M, A_H) = C_M\,\Delta x\,\Delta y\,\frac{1}{2}\left[\left(\frac{\partial U}{\partial x}\right)^2 + \frac{1}{2}\left(\frac{\partial V}{\partial x} + \frac{\partial U}{\partial y}\right)^2 + \left(\frac{\partial V}{\partial y}\right)^2\right]^{1/2} \quad , \tag{18}$$

where C_M is a constant which should be chosen as small as possible, but large enough to filter out noise at the shortest wavelengths. For the simulations presented here, $C_M = 0.2$. To preserve sharp fronts in the density field, the horizontal diffusivity is chosen as $A_H = 0$.

3.2.1 Vertical eddy viscosity, K_M, and diffusivity, K_H

To close the system of equations given in 3.2, the 2 1/2 level Mellor and Yamada (Mellor & Yamada 1982) turbulence closure scheme, with modifications due to (Galperin, Kantha, Hassid & Rosati 1988), is used to compute the vertical eddy viscosity, K_M, and the vertical eddy diffusivity, K_H, which are functions of turbulent kinetic energy, $q^2/2$, and turbulent macro scale, l. The governing equation for $q^2/2$ and l are

$$\frac{\partial q^2}{\partial t} + \vec{U} \cdot \nabla q^2 + W \frac{\partial q^2}{\partial z} = \frac{}{\partial z}\left(K_q \frac{\partial q^2}{\partial z}\right) + 2K_M \left[\left(\frac{\partial U}{\partial z}\right)^2 + \left(\frac{\partial V}{\partial z}\right)^2\right] + \frac{2g}{\rho_0} K_H \frac{\partial \rho}{\partial z} - \frac{2q^3}{B_1 l} \quad , \tag{19}$$

and

$$\frac{\partial q^2 l}{\partial t} + \vec{U} \cdot \nabla q^2 l + W \frac{\partial q^2 l}{\partial z} = \frac{}{\partial z}\left(K_q \frac{\partial q^2 l}{\partial z}\right) + lE_1 K_M \left[\left(\frac{\partial U}{\partial z}\right)^2 + \left(\frac{\partial V}{\partial z}\right)^2\right] + \frac{lE_1 g}{\rho_0} K_H \frac{\partial \rho}{\partial z} - \frac{q^3}{B_1} \tilde{W} \quad , \tag{20}$$

where

$$\tilde{W} = 1 + E_2 \left(\frac{l}{\kappa L}\right)^2 \quad , \tag{21}$$

and

$$L^{-1} = (\eta - z)^{-1} + (H + z)^{-1} \quad . \tag{22}$$

$\kappa = 0.4$ is the von Karman constant. From stability analysis the stability functions become

$$S_M[1 - 9A_1A_2G_H] - S_H[18A_1^2 + 9A_1A_2G_H] = A_1[1 - 3C_1 - 6A_1/B_1] \quad , \tag{23}$$

and

$$S_H[1 - (3A_2B_2 + 18A_1A_2)G_H] = A_2[1 - 6A_1/B_1] \quad , \tag{24}$$

defining G_H as

$$G_H = \frac{l^2}{q^2} \frac{g}{\rho_0} \frac{\partial \rho}{\partial z} \quad , \tag{25}$$

and the empirical values

$$(A_1, A_2, B_1, B_2, C_1, E_1, E_2) = (0.92, 0.74, 16.6, 10.1, 0.08, 1.8, 1.33) \quad . \tag{26}$$

K_M and K_H are then computed according to

$$K_M = lqS_M \quad , \tag{27}$$
$$K_H = lqS_H \quad , \tag{28}$$
$$K_q = 0.20lq \quad . \tag{29}$$

The empirical values are derived from large water tank experiments, and whether these values are representative for the ocean is not clear. To avoid instabilities, minimum values for K_M and K_H are set to $1 \times 10^{-5}\,\mathrm{m^2\,s^{-1}}$ and $1 \times 10^{-7}\,\mathrm{m^2\,s^{-1}}$ respectively.

3.2.2 Boundary conditions

At the free surface, $z = \eta(x, y)$, the boundary conditions are:

$$\rho_0 K_M \left(\frac{\partial U}{\partial z}, \frac{\partial V}{\partial z}\right) = (\tau_{0x}, \tau_{0y}) \quad , \tag{30}$$
$$\rho_0 K_H \left(\frac{\partial T}{\partial z}, \frac{\partial S}{\partial z}\right) = (\dot{T}_0, \dot{S}_0) \quad , \tag{31}$$
$$q^2 = B_1^{2/3} u_{\tau 0} \quad , \tag{32}$$
$$l = 0 \quad , \tag{33}$$

where $(\tau_{0x}, \tau_{0y}) = \vec{\tau}$ is the wind stress, $\dot{T}_0$ is surface heat flux, $\dot{S}_0$ is net precipitation/evaporation (including river run off and freezing/melting of sea ice) and $u_{\tau 0} = (\vec{\tau_0^2})^{1/2}$.

There are no volume fluxes allowed through the side walls, and free slip conditions for the flow are applied. There are no advective or diffusive heat and salt fluxes on the side walls or at the bottom of the basin. The kinematic boundary condition gives

$$W_0 = U\frac{\partial \eta}{\partial x} + V\frac{\partial \eta}{\partial y} + \frac{\partial \eta}{\partial t}, \quad z = \eta(x, y, t), \tag{34}$$
$$W_b = -U_b\frac{\partial H}{\partial x} - V_b\frac{\partial H}{\partial y}, \quad z = -H(x, y). \tag{35}$$

The effect of bottom drag on horizontal velocities is given by

$$\rho_0 K_M \left(\frac{\partial U}{\partial z}, \frac{\partial V}{\partial z}\right) = (\tau_{bx}, \tau_{by}) \quad , \tag{36}$$
$$\tag{37}$$

where the bottom stress, $\vec{\tau}_b = (\tau_{bx}, \tau_{by})$, is specified by

$$\vec{\tau}_b = \rho_0 C_D |\vec{U}_b| \vec{U}_b, \tag{38}$$

and the drag coefficient C_D by

$$C_D = \max \left[0.0025, \frac{\kappa^2}{(ln(z_b/z_0))^2} \right] \quad . \tag{39}$$

Here z_b is the nearest grid point to the bottom, $z_0 = 0.01m$ is the roughness parameter (Weatherly & Martin 1978), and $\kappa = 0.4$ is the von Karman constant. At the bottom the turbulent kinetic energy and the turbulent macro scale is given by

$$q^2 = B_1^{2/3} u_{\tau b} \quad , \tag{40}$$

$$l = 0, \tag{41}$$

where $u_{\tau b} = (\vec{\tau}_b^2)^{1/2}$.

3.3 The σ-coordinate model

The basic equations have been transformed into a so-called σ-coordinate system. This is a bottom and surface following coordinate system that has the property that the bottom always has the σ-coordinate -1 and the free surface always has the σ-coordinate 0. The transformation from the Cartesian coordinate system (x, y, z, t) to the σ-coordinate system (x^*, y^*, σ, t^*) is given by

$$x^* = x \quad y^* = y \quad \sigma = \frac{z-\eta}{\eta+H} \quad t^* = t$$

where $\eta(x, y, t)$ is the surface elevation and $H(x, y)$ is the depth measured from the surface at rest. Normalising the difference between the vertical position z and the surface elevation η with the total depth of the water column $D = H + \eta$ gives the bottom following σ-coordinate which ranges from $\sigma = 0$ at $z = \eta$ to $\sigma = -1$ at $z = -H(x, y)$. The transformation from the Cartesian coordinate system to the σ-coordinate system introduces several new terms in equations 16 and 17, which are neglected according to Mellor & Blumberg (1985). The governing equations in σ-coordinates, in flux form, are given by Berntsen (2000).

3.4 Time splitting

External gravity waves require short time steps in order to represent these waves and their effects accurately. The internal waves include reduced gravity

and the corresponding time step can be much longer, typically 30 times larger. This problem can be solved by using a implicit scheme or by assuming a rigid lid. However, time integration can also be split into a two dimensional external (barotropic) mode, solving for surface elevation and depth averaged velocities, and a three dimensional internal (baroclinic) mode, solving for depth dependent velocities, temperature, salinity and turbulence.

3.5 Numerical interpretations of the governing equations

The governing equations form a set of simultaneous partial equations that not can be solved using any known analytical methods. The equations in 3.2 have therefore been solved using finite difference methods, with an Arakawa C-grid (Mesinger & Arakawa 1976), a staggered horizontal scheme, Figure 1. Scalar fields such as S, T and RHO are defined in S-points, while KM, KH and $Q2L$ are defined in W-points. The depth integrated velocities (the 2D fields) and η are given at cell interfaces and cell centres respectively.

BOM is written in FORTRAN 90, and the discrete versions of the state variables and parameters are declared in a module, STATE, that may be addressed by all subroutines. The basic equations transformed into a bottom following sigma coordinate system, Section 3.3, are stepped forward in time based on the method of fractional steps, using the same time step for all equations. A sequence of subroutines is called to perform specific subtasks and to update the corresponding variables in MODULE STATE at each time step. After all subroutines are called, the effects of all terms in the governing equations are included.

3.6 Essential BOM routines

For each 3-D time step, forcing fields such as atmospheric, river runoff and tidal forcing are computed, before DENS is called to update the density field from S and T, where after MY2HALV propagates Q^2 and Q^2l and computes K_M, K_H and K_q. However, K_M and K_H can not be less than K_MMIN and K_HMIN respectively, to avoid instability, but at the same time it is important to keep these minimum values low to maintain the density structure in the ocean as well as possible. Minimum values for K_M and K_H are set to $1\text{x}10^{-5}\,\text{m}^2\,\text{s}^{-1}$ and $1\text{x}10^{-7}\,\text{m}^2\,\text{s}^{-1}$ respectively. UPSTREAMQ advects q^2 and q^2l in equation 19 and 20 with the upstream method, and BOUND updates the q^2 and q^2l fields at the open boundaries and saves the water level from the previous time step. INTERNAL then calculates the effects of

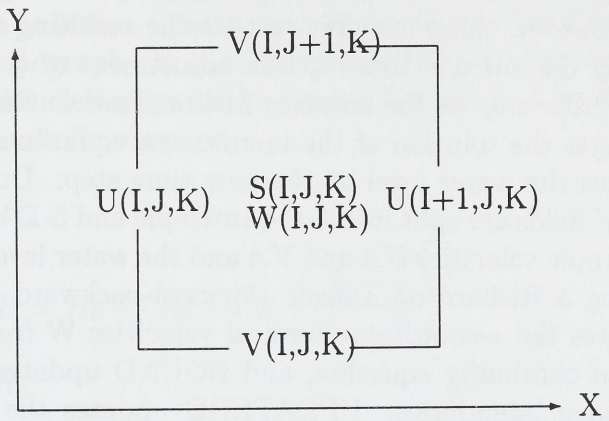

(a) Horizontal view

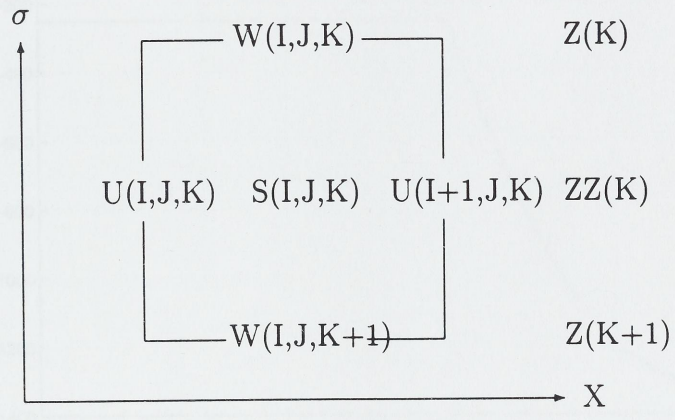

(b) Vertical view

Figure 1: The location of 3D variables in the C-grid. T, ρ and other scalar fields are defined in S-points. Z is the σ-coordinate at the cell interface, and ZZ is the σ-coordinate at the cell center.

internal pressure on the momentum, before LAXWUV estimates the effects of advection on the momentum. Internal pressure force is difficult to approximate in areas with steep topography when using σ-coordinate models. The worst case scenario is when the σ-surfaces intercept iso-surfaces of density at right angles. However, there is evidence that the resulting large and erroneous currents may die out due to advective adjustment of the density field in prognostic experiments, see for instance Mellor, Ezer & Oey (1994). MODESPLIT propagates the solution of the momentum equations one 3-D time step and estimates the water level at the new time step. During this subroutine the U and V fields are split into 2-D barotropic and 3-D baroclinic parts, where the barotropic velocities UA and VA and the water level is propagated $N2D$ step using a Richardson scheme (forward-backward method). Then WREAL computes the z-coordinate vertical velocities W from the σ-coordinate transformed continuity equation, and BOUND updates the 3-D velocity filed at the open boundaries. UPDATEDD updates the dynamic depths of the model, and SUPERBEEF advects the S and T fields, and, if $C_H \neq 0$, computes the horizontal diffusion.SUPERBEEF also computes the surface fluxes of S and T, $SSURF$ and $TSURF$, respectively.

VERTDIFF computes the vertical diffusion of the S and T fields, whereas BOUND updates the S and T fields at open boundaries. OUTPUT gives the model output.

4 Model setup

The model is of a two dimensional vertical section with 3 grid cells along-shelf and 400 grid cells cross-shelf and 50 vertical σ-layers. The horizontal grid resolution is 500 m. There is no atmospheric, Coriolis or tidal forcing. The bottom topography is an idealised shelf slope (Ommundsen 2000), which resembles the shelf slope at the Ormen Lange block west of Ålesund, described by the parabolic equation

$$H = \begin{cases} H_s & 0 \leq y \leq S_1 \\ H_0 - (H_0 - H_s)\left(\dfrac{S_2 - y}{S_2 - S_1}\right)^2 & S_1 < y < S_2 \\ H_0 & S_2 \leq y \leq L_y \end{cases} \tag{42}$$

where $H_0 = 250\,\text{m}$, $H_s = 1300\,\text{m}$, $LL = 160\,\text{km}$, $LS = 60\,\text{km}$ and $x = 200\,\text{km}$. The profile is shown in Figure 2. The shelf profile has a discontinuity at the

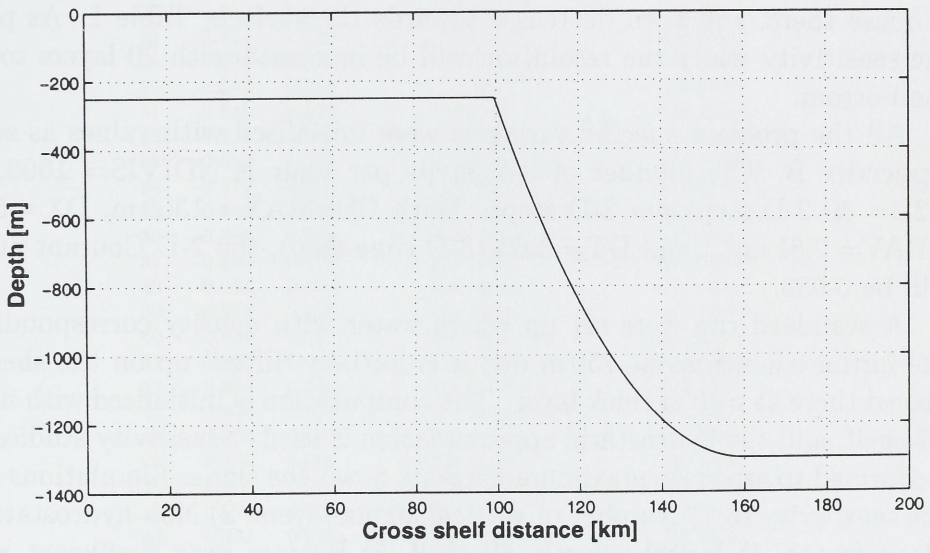

Figure 2: **The idealised shelf slope.**

shelf edge and the mean slope factor from shelf edge down to 750 m is 0.033.

The stratification is taken from climatology and is for simplicity chosen to be horizontally uniform. The justification for this is that the focus here is not on large scale oceanographic phenomena, but on local dynamics.

At both ends of the domain, there are open boundaries, where the FRS-relaxation technique of Martinsen & Engedahl (1987) is used. The relaxation

zone is 15 grid cells wide. In the upstream boundary zone, 2-D and 3-D velocities are relaxed towards different boundary conditions, however they are always equal to the initial conditions. The boundary conditions for the 3-D velocities are always zero, while the initial conditions for the 2-D velocity field will vary in the sensitivity tests. Also in the downstream boundary zone, the 2-D and the 3-D velocities are relaxed towards different boundary conditions, but here the boundary conditions vary throughout the simulation run, depending on average velocities some grid cells upstream of the relaxation zone. Each prognostic variable , ϕ, is updated in the relaxation zone according to the formulae

$$\phi = (1 - \alpha)\phi_M + \alpha\phi_F \quad , \tag{43}$$

where ϕ_M contains the unrelaxed values computed by the model and ϕ_F is the specified solution in the zone. The α's are calculated with a tanh function and vary between 1 at the model boundary and 0 at the end of the relaxation zone.

Since the focus is on phenomena near the bottom, the vertical resolution is dense there, and then decreases towards the surface, Table 1. As part of the sensitivity study the resolution will be increased with 20 layers towards the bottom.

All the problem specific variables were initialised with values as seen in Appendix B. The number of 3-D steps per hour is NDIVIS= 1000, with N2D= 30 2-D steps per 3-D steps. With DEPMAX= 1300 m, DX= 500 m, GRAV= 9.81 ms^{-1} and DT= 3.6 s (3-D time step), the 2-D Courant number will be 0.083.

A standard run were set up where water with density corresponding to the initial conditions at 750 m depth is initially 'lifted' up on the shelf and placed there as a 50 m thick layer. The computation is initialised with no flow off-shelf, and the hydrostatic approximation is used. Sensitivity studies were performed to estimate maximum currents down the slope. Simulations where the sensitivity to 1) Number of vertical sigma layers, 2) Non-hydrostatics, 3) Slope factor, 4) Initial velocity off shelf, 5) Bottom drag coefficient and 6) Shelf edge profile were performed.

K	Z	DZ	σ-depth at 250 m	σ-depth at 750 m
1	0.000	0.058	0	0
2	-0.058	0.056	-14.5000	-43.5000
3	-0.113	0.053	-28.2500	-84.7500
4	-0.167	0.051	-41.7500	-125.2500
5	-0.218	0.049	-54.5000	-163.5000
6	-0.267	0.047	-66.7500	-200.2500
7	-0.314	0.045	-78.5000	-235.5000
8	-0.359	0.043	-89.7500	-269.2500
9	-0.402	0.041	-100.5000	-301.5000
10	-0.443	0.039	-110.7500	-332.2500
11	-0.481	0.036	-120.2500	-360.7500
12	-0.518	0.034	-129.5000	-388.5000
13	-0.552	0.032	-138.0000	-414.0000
14	-0.584	0.030	-146.0000	-438.0000
15	-0.614	0.028	-153.5000	-460.5000
16	-0.642	0.026	-160.5000	-481.5000
17	-0.668	0.024	-167.0000	-501.0000
18	-0.692	0.022	-173.0000	-519.0000
19	-0.714	0.020	-178.5000	-535.5000
20	-0.734	0.018	-183.5000	-550.5000
21	-0.751	0.015	-187.7500	-563.2500
22	-0.766	0.013	-191.5000	-574.5000
23	-0.780	0.011	-195.0000	-585.0000
24	-0.791	0.009	-197.7500	-593.2500
25	-0.800	0.008	-200.0000	-600.0000
26	-0.808	0.008	-202.0000	-606.0000
27	-0.816	0.008	-204.0000	-612.0000
28	-0.824	0.008	-206.0000	-624.0000
29	-0.832	0.008	-208.0000	-624.0000
30	-0.840	0.008	-210.0000	-630.0000
31	-0.848	0.008	-212.0000	-636.0000
32	-0.856	0.008	-214.0000	-642.0000
33	-0.864	0.008	-216.0000	-648.0000
34	-0.872	0.008	-218.0000	-654.0000
35	-0.880	0.008	-220.0000	-660.0000
36	-0.888	0.008	-222.0000	-666.0000
37	-0.896	0.008	-224.0000	-672.0000
38	-0.904	0.008	-226.0000	-678.0000
39	-0.912	0.008	-228.0000	-684.0000
40	-0.920	0.008	-230.0000	-690.0000
41	-0.928	0.008	-232.0000	-696.0000
42	-0.936	0.008	-234.0000	-702.0000
43	-0.944	0.008	-236.0000	-708.0000
44	-0.952	0.008	-238.0000	-714.0000
45	-0.960	0.008	-240.0000	-720.0000
46	-0.968	0.008	-242.0000	-726.0000
47	-0.976	0.008	-244.0000	-732.0000
48	-0.984	0.008	-246.0000	-738.0000
49	-0.992	0.008	-248.0000	-744.0000
50	-1.000	0.000	-250.0000	-750.0000

Table 1: *K is the Sigma-layer, Z is the σ-coordinates of cell interfaces, DZ is the thickness in σ-coordinates of cells. The following two columns give the σ-depths for 250 m and 750 m depth respectively.*

5 Results

All simulations were run for 20 hours. This seems sufficient for the plume of dense water to advect down the slope. Figure 3 shows the initial density distribution. Water with a density equal to about 1028.1 kgm^{-3} is elevated from 750 m depth up on the shelf as a 50 m thick layer from 200 to 250 m depth. The surrounding water at the shelf has density of about 1027.5 kgm^{-3}. This will be the initial density distribution for all simulations unless otherwise specified. As a result of the routine generating iso lines of density, based on one single representative density profile, the iso lines of density may seem rather artificial above the shelf slope close to the surface. This should however not influence the results significantly.

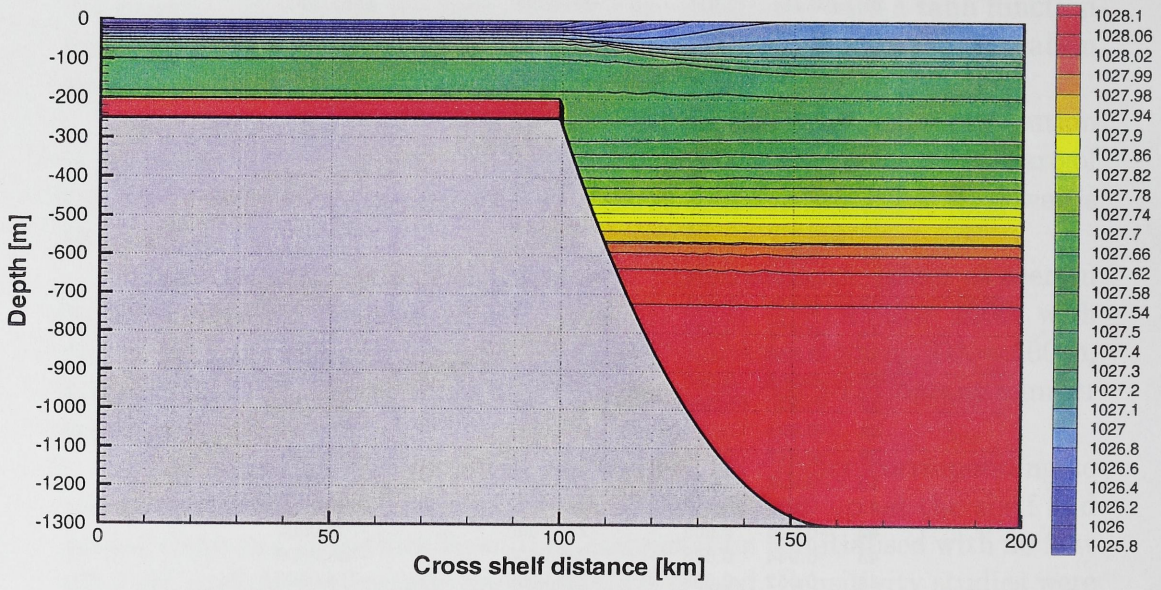

Figure 3: *Initial density distribution.*

5.1 Standard run

As the simulation starts, the plume of dense water elevated to the shelf accelerates down the shelf slope, Figures 4 and 5. The density difference between the plume and the surrounding water decreases, both because the plume moves towards a level of equal density and because of entrainment of surrounding water. This will decrease the driving force (differences in gravity

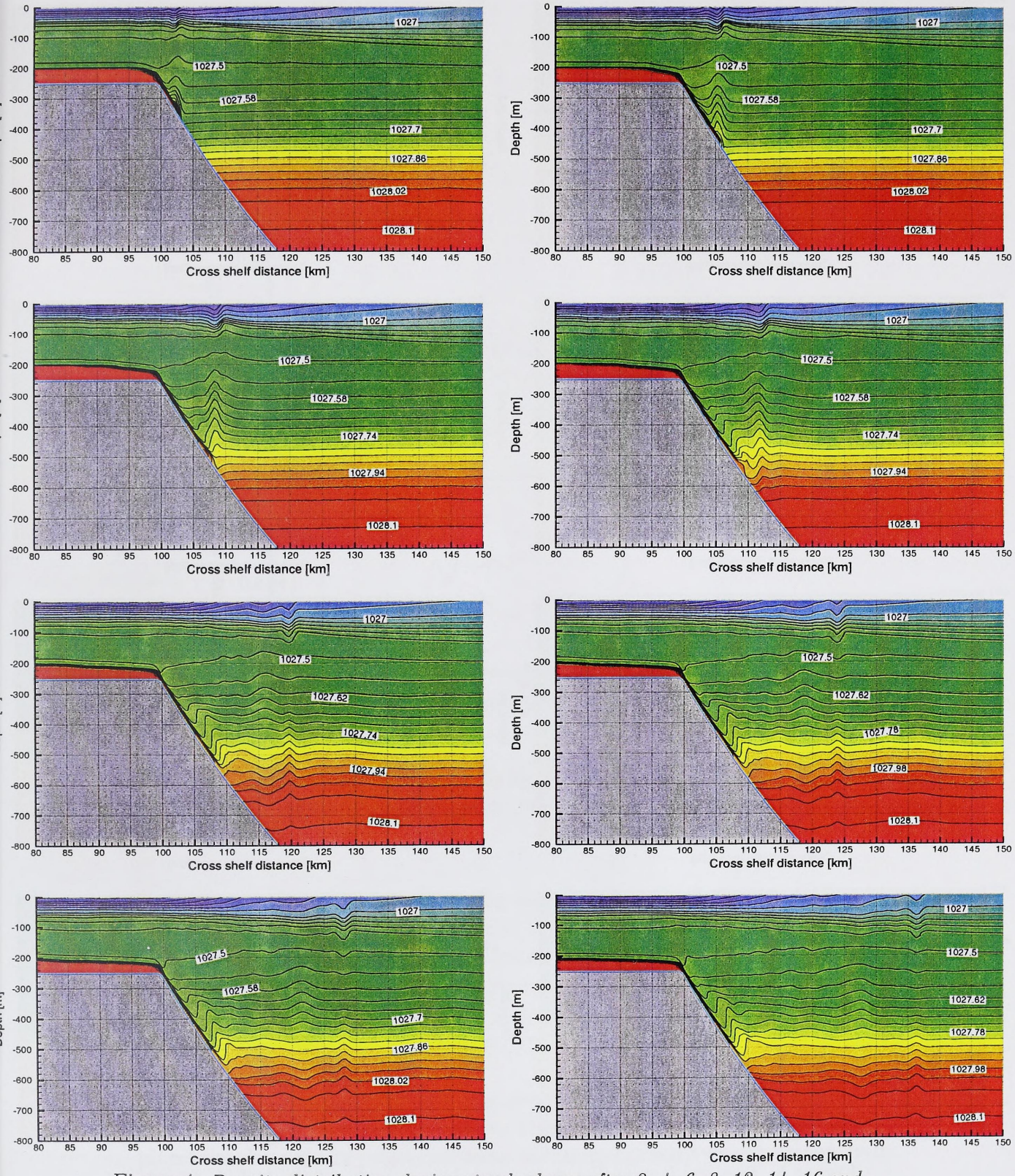

Figure 4: *Density distribution during standard run after 2, 4, 6, 8, 12, 14, 16 and 20 hours.*

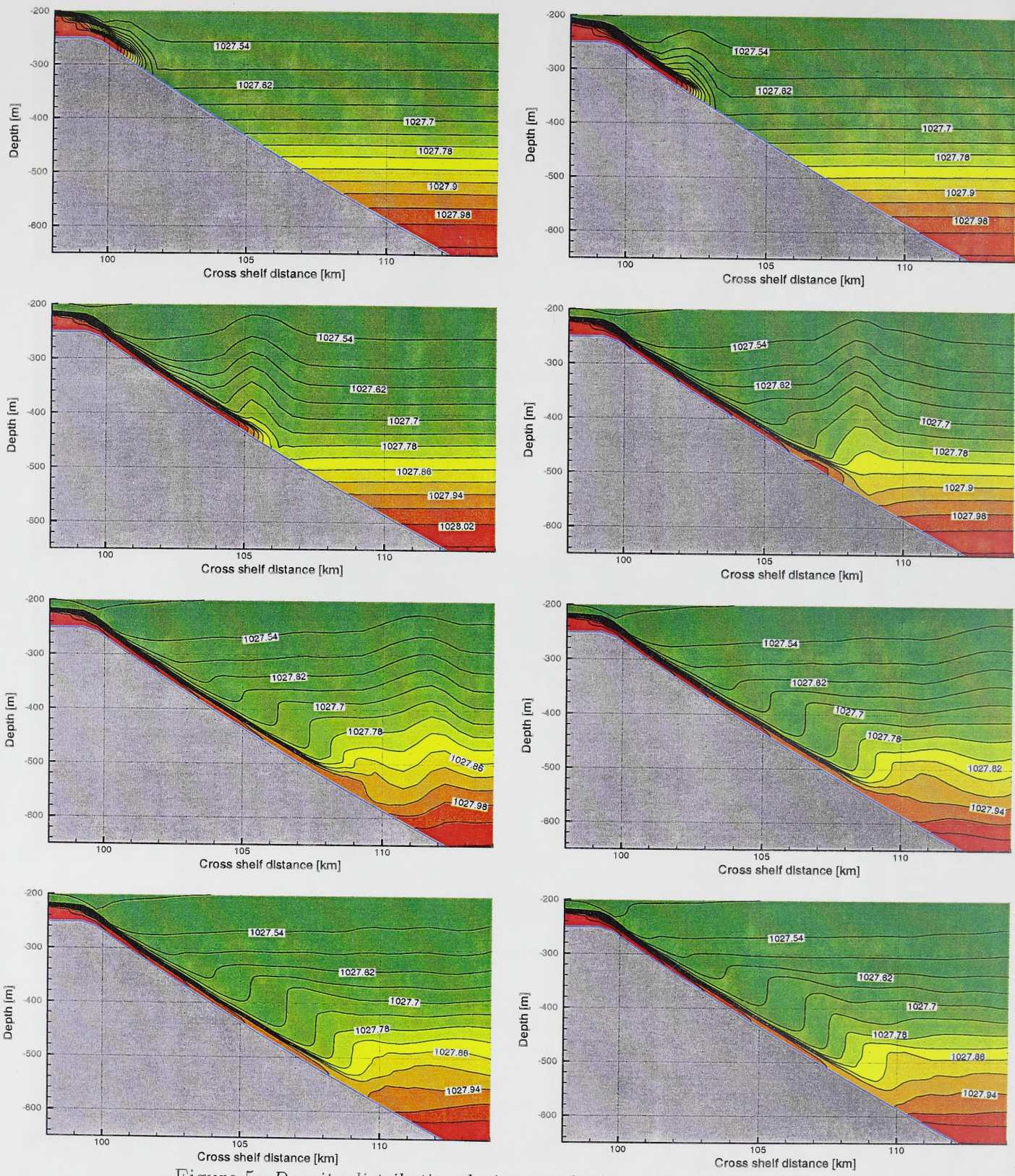

Figure 5: *Density distribution during standard run after 1, 2, 4, 6, 8, 10, 12 and 16 hours.*

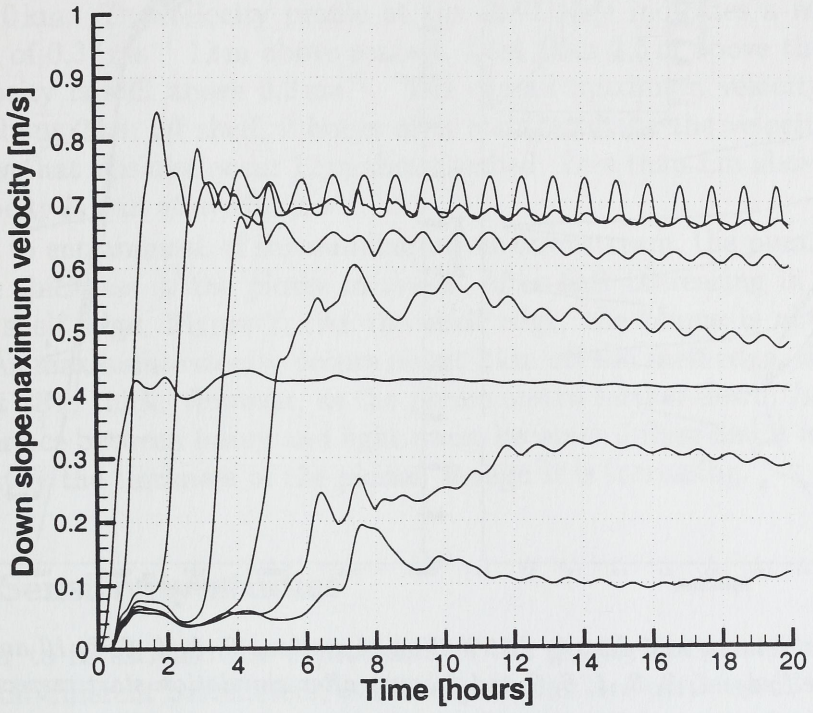

Figure 6: *Timeserie of maximum velocity in the water column at stations 0, 2, 4, 6, 8, 10 and 12 km off the shelf edge. Maximum velocity occur in cronological order.*

force between plume and surrounding water) and give a new level of neutral buoyancy at about 600 m depth (about 1027.9 kgm^{-3}), 150 m above the level where the water initially was taken from.

As the plume flows down shelf slope, the surrounding water is pertubed, and internal waves are generated. A quick estimate based on the figures, indicate a wave propagation of about 2 ms^{-1}, which fits well with the speed of internal gravity waves, $\sqrt{g^{\star}H}$.

From the figures it can also be seen that the plume undershoots the equilibrium level due to momentum. The excess energy available when the plume decelerates will propagate away as internal gravity waves, though part of it will generate turbulence.

It can also be seen that due to continuity, there is an upstream flow of water above the gravity current with significantly lower velocity. This is a distinct signal in the vertical density distribution 8 hours after start and

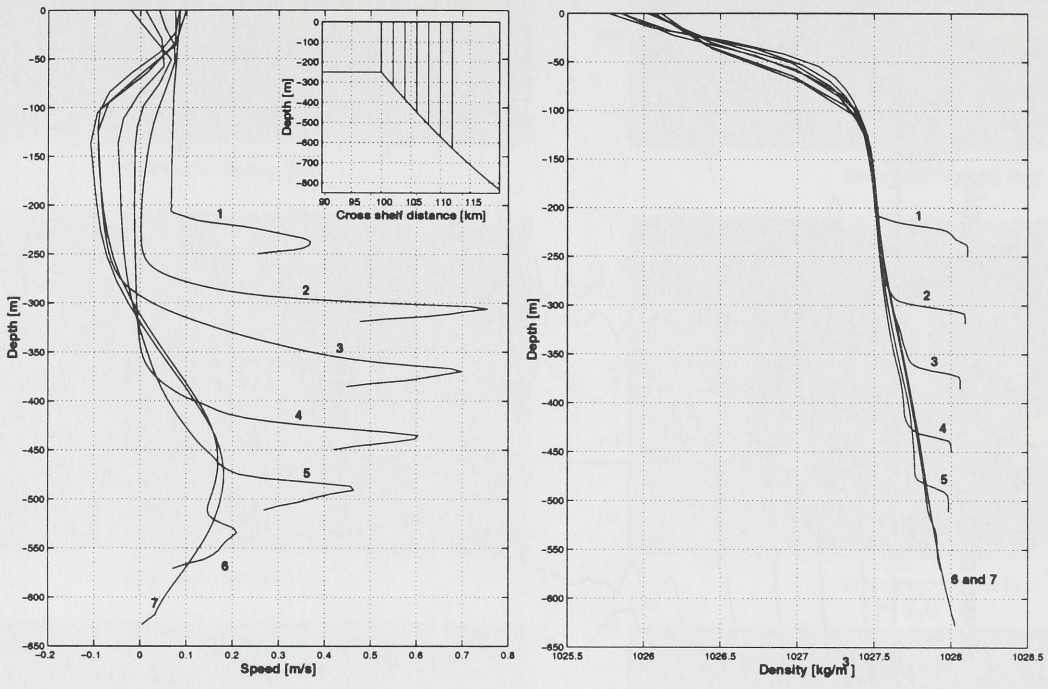

Figure 7: *Velocity and density distribution at stations 0, 2, 4, 6, 8, 10 and 12 km off the shelf edge 1, 2, 3, 4, 6, 7 and 8 hours after simulation start respectively.*

later. Figure 6 shows time series of down slope velocities, the maximum in each water column, at the locations shown as a sub-figure in Figure 7; 0, 2, 4, 6, 8, 10 and 12 km off the shelf edge. It is clear that the maximum velocity occurs some 2 km off the shelf edge. This is plausible considered what is earlier mentioned about entrainment and decreasing density differences down slope. The maximum velocity is about $0.85\,\mathrm{ms}^{-1}$ and occurs after 1 hour and 51 minutes. As the head of the plume passes the station, the velocity decreases, varying between 0.65 and $0.75\,\mathrm{ms}^{-1}$. The fluctuation we observe in the time series may be associated with the hydrostatic assumption and the discontinuous shelf edge. This is supported by Figure 9, where the fluctuations dissappear when running non-hydrostatically and while replacing the discontinuous shelf edge with a continuous one, and the fact that the fluctuations increase with increasing slope and thereby the difference in slope at each side of the discontinuity. The fluctuations are larger closer to the shelf edge, where the density difference is greatest.

Figure 7 show the velocity and density profile of the plume head at the locations indicated by the sub-figure, during local maximum velocity, 1, 2, 3, 4, 6, 7 and 8 hours after start. The speed of the gravity current decreases downstream and it takes about 8 hours for the head to reach the level of

equal density. This gives a distinct decrease in down slope velocity from the stations more than 8 km off shelf. The total travel distance of the flow is about 10 km. The velocity profile at the shelf edge indicates a maximum velocity of 0.37 ms^{-1} 12 m above seabed. Less than 2.5 m above the seabed the velocity is still above 0.3 ms^{-1}. The overall maximum velocity can be found about 2 km off shelf, 2 hours after start, and the the velocity profile indicates that this also occur 12 m above seabed. Less than 1 m above seabed the velocity is still above 0.5 ms^{-1}.

Due to entrainment of surrounding water downstream, the plume dilutes and the thickness of the plume increases, after first decreasing in size just off the shelf edge, Figure 7. At the shelf edge, the plume is about 42 m thick. As maximum velocity occurs about 2 km off the shelf edge, the plume is about 25 m thick. However, as the plume moves further down the incline, the interface between heavy and light water becomes diffuse and it is difficult to quantify the thickness of the plume, though it is increasing.

5.2 Sensitivity studies

In order to investigate the dependence of the gravity current velocity and profile on different parameters, sensitivity studies are performed. Only one parameter deviates from the standard run for each of these simulations. The sensitivity simulations include 1) increasing the number of vertical sigma layers, 2) introducing non-hydrostatic physics, 3) varying the initial velocity off shelf, 4) changing the shelf edge profile 5) increasing the slope factor and finally 6) decreasing the drag coefficient. Figures with vertical sections of time development of the density for test cases 1, 2, 3, 5, 6 are presented in Appendix B. Figures showing time series of velocity and the profile of velocity and density at different stations down the shelf slope is included in this section. The profiles of velocity and density are taken as close as possible to the head at each station. Table 2 gives the times where the profiles were taken.

5.2.1 Increasing the vertical resolution

Increasing the vertical resolution by 20 σ-layers, while holding the initial velocity off shelf fixed (0 ms^{-1}), alters the velocity and the shape of the gravity current. Figure 11 deviates distinctly from Figure 5 six hours after start. In the standard run the head seems to separate from the body shortly before reaching the level of neutral buoyancy. Increasing the number of σ-layers to 70, shows that this feature is a numerical misrepresentation due to

Simulation	Time of profile				
	0 km	2 km	4 km	6 km	8 km
Standard	1	2	4	5	6
Vertical resolution	1	2	4	5	6
Non-hydrostatics	1	3	5	6	8
Slope factor	1	2	4	5	6
Initial velocity $U = 0.1\,\mathrm{ms}^{-1}$	1	2	4	5	6
$U = 0.2\,\mathrm{ms}^{-1}$	1	2	4	5	6
Drag coefficient	1	2	3	3	4
Shelf profile	1	2	3	4	5

Table 2: *Logging time of profiles at the different stations.*

insufficient vertical resolution. The same figures also shows that the plume is more diluted when simulated with 50 σ-layers instead of 70.

However, the maximum velocity occurs at the same location, with the same value and at the same time as during the standard run, Figure 8b. At the same time the oscillations of the time series of maximum velocity are now more distinct, though still decreasing in amplitude going off shelf.

Figures 9b and 10b show velocity and density profiles during local maximum velocity at locations 0, 2, 4, 6, and 8 km off shelf, as indicated in the subfigure 9a. The profiles are taken approximately as the head of the gravity current passes by the respective stations, Table 2. The velocity profile is more preserved as a gravity current with 70 σ-layers than during the standard run. Also, the velocity towards the seabed is higher with improved vertical resolution. The results indicate that insufficient vertical resolution of the phenomenon increases the eddy viscosity. The density profiles show more or less the same features as with 50 σ-layers.

5.2.2 Introducing non-hydrostatic physics

In many numerical ocean models, the hydrostatic approximation is made. This approximation causes a considerable saving in computing time. The simulations including non-hydrostatic physics in this report, require twice as much computing time as the other the simulations. However, if one wants to increase the grid resolution and resolve phenomena on small scale, as for gravity currents, the approximation becomes questionable. With improvements in computing power, it becomes possible to avoid using the hydrostatic approximation. Investigating time and length scales then becomes necessary

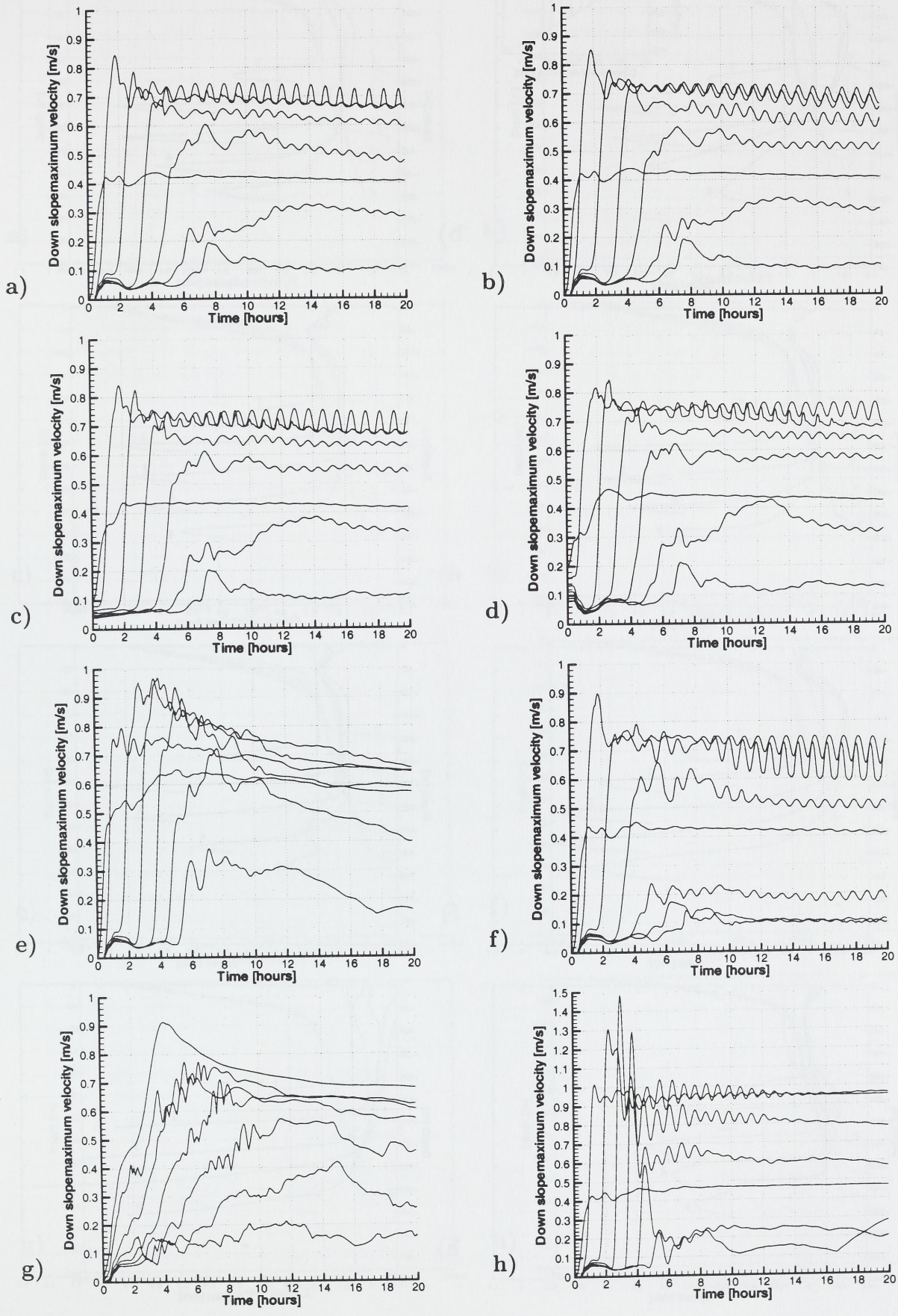

Figure 8: *Timeserie of velocity 0, 2, 4, 6, 8, 10 and 12 km off the shelf edge. a) Standard run, b) With 70 σ-layers, c) Initial velocity off shelf $U = 0.1\,ms^{-1}$, d) Initial velocity off shelf $U = 0.2\,ms^{-1}$, e) New shelf edge profile, f) Slope factor equal to 0.04, g) Includes non-hydrostatic physics and h) Drag coefficient $C_D = 0$.*

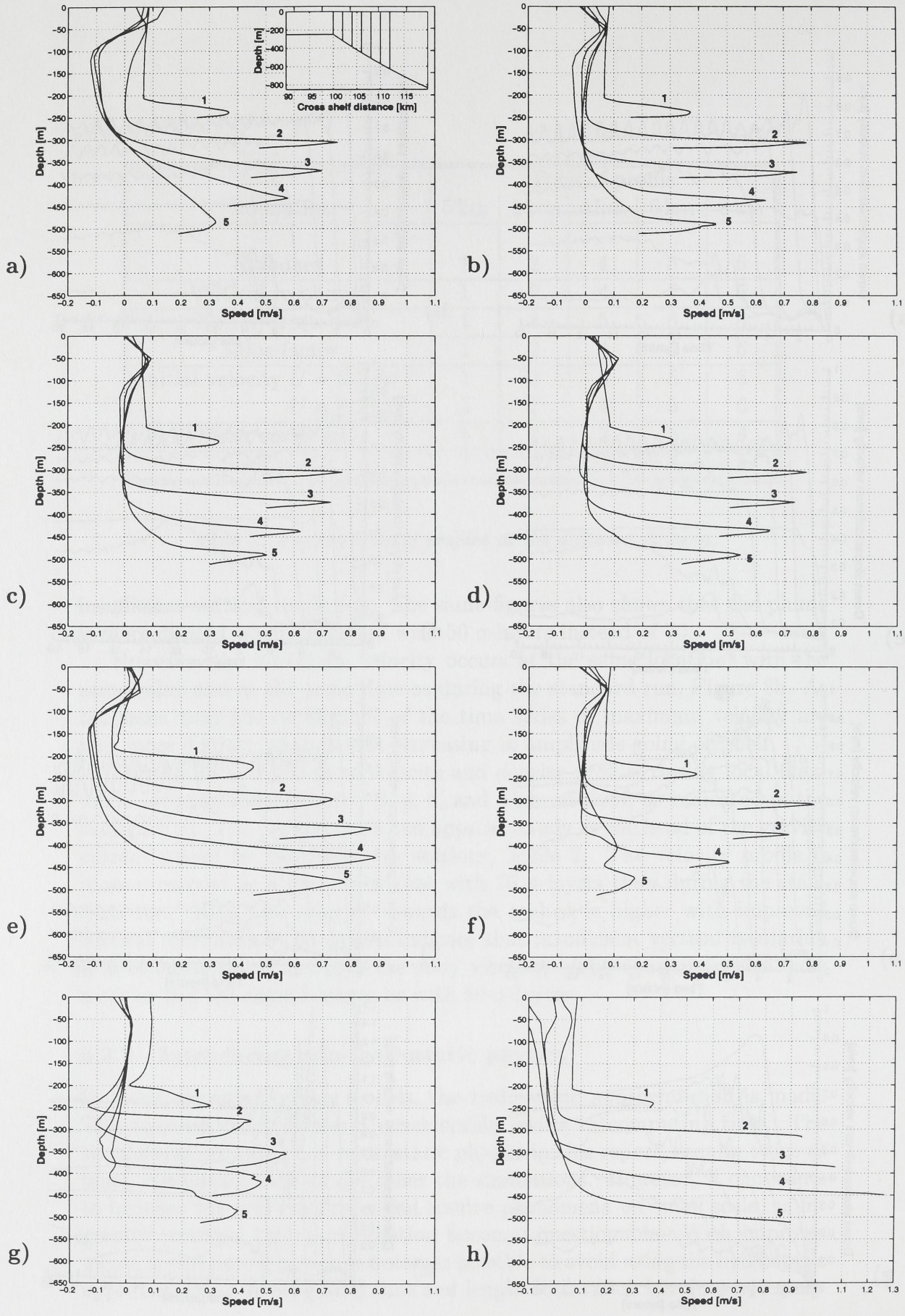

Figure 9: *Velocity profile as the head passes the stations. a) Standard run, b) With 70 σ-layers, c) Initial velocity off shelf $U = 0.1\,ms^{-1}$, d) Initial velocity off shelf $U = 0.2\,ms^{-1}$, e) New shelf edge profile, f) Slope factor equal to 0.04, g) Includes non-hydrostatic physics and h) Drag coefficient $C_D = 0$.*

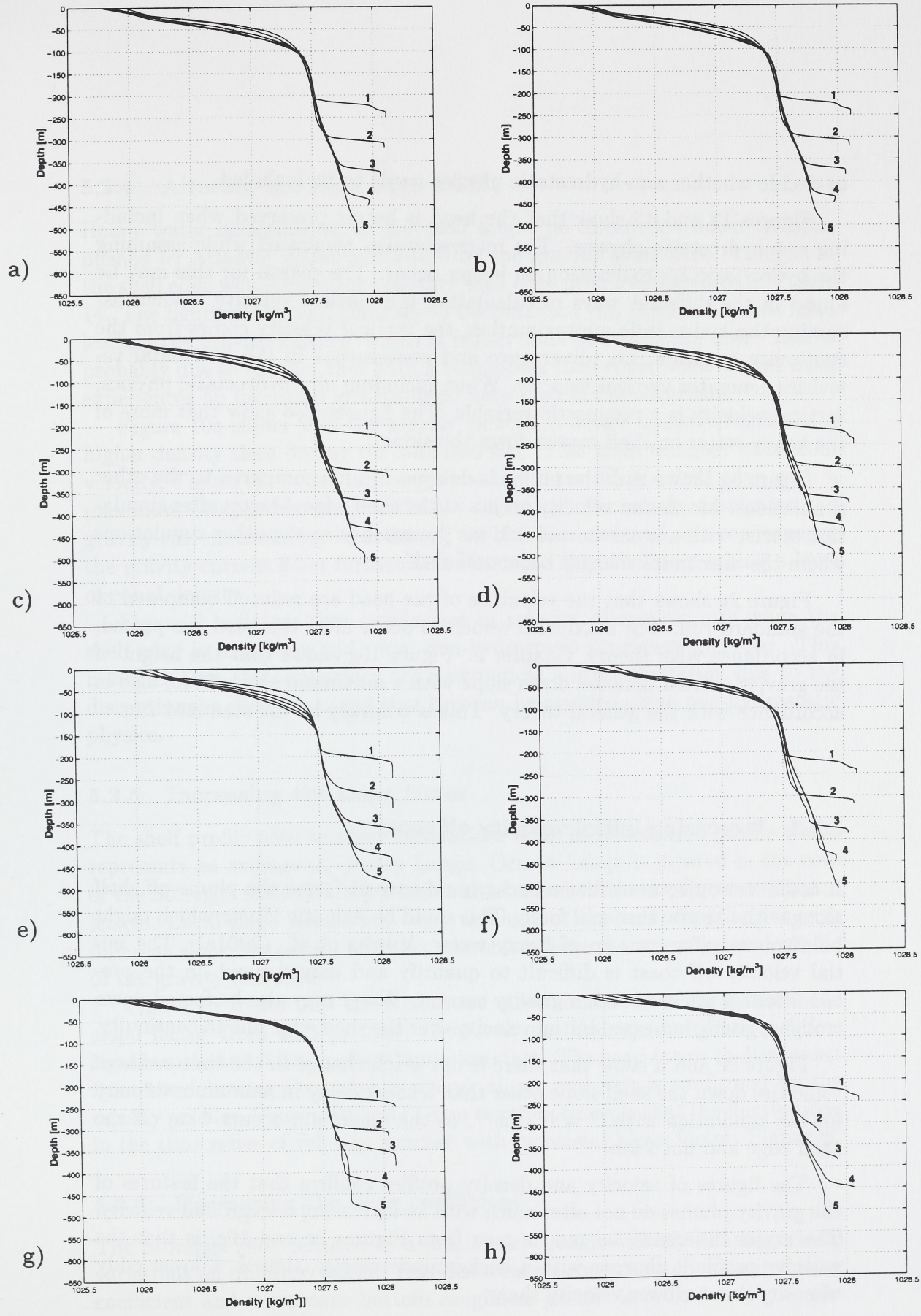

Figure 10: *Density profile as the head passes the stations. a) Standard run, b) With 70 σ-layers, c) Initial velocity off shelf $U = 0.1\,ms^{-1}$, d) Initial velocity off shelf $U = 0.2\,ms^{-1}$, e) New shelf edge profile, f) Slope factor equal to 0.04, g) Includes non-hydrostatic physics and h) Drag coefficient $C_D = 0$.*

to decide whether non-hydrostatic physics needs to be included.

Figures 12 and 13 show that the head is better preserved when including non-hydrostatic physics. The internal waves generated while assuming the hydrostatic approximation no longer occur. The reason for this may be found in the different ways of calculating the vertical velocity. When assuming the hydrostatic approximation, the vertical velocity comes from the continuity equation, i.e. divergence and convergence in the horizontal velocities generates vertical velocity. When including non-hydrostatic physics, vertical velocity is a prognostic variable. The figures also show that more of the heavy water on shelf moves down the slope.

Figure 8g shows that the plume is delayed in time compared to the other simulations. Maximum velocity occurs at the shelf edge 4 hours after simulation starts, with a maximum of $0.91\,\mathrm{ms}^{-1}$, contrary ro the other simulations where the maximum velocity occurs off shelf.

Figure 9g shows that the velocities of the head are reduced compared to the standard run. The maximum velocities occur after the head has passed, in accordance with theory, Chapter 2. Figure 10g shows that the height of the gravity current increase down slope with a maximum above 50 m, also in accordance with the general theory. This is contrary to the standard run.

5.2.3 Increasing initial velocity off coast

It could be conjectured that a background current forces the plume off shelf along with the gravitational force. This could be Atlantic Water which might be displaced after run up of heavy water, Vikebø et al. (2001a). The initial velocity off coast is difficult to quantify and may depend on the preconditioning phase of such a gravity current. Water may also be forced down troughs, giving increased initial velocity over the shelf edge due to continuity.

Figure 8c and d show that there is not much change in the time series of velocities down the shelf slope other than a short delay in maximum velocity for the simulation with $U = 0.2\,\mathrm{ms}^{-1}$, as the maximum occurs 4 km off the shelf edge and not 2 km.

The figures of velocity and density profiles confirm that the features of the gravity plumes do not alter much with an increasing background velocity. The major difference, as can be seen from Figures 9c and 10c, is that the velocity profile is sharper with a background velocity, that is, a lower eddy viscosity due to lower velocity shear.

5.2.4 Altering the shelf edge profile

Heavy water displaced on to the shelf might be channelled down troughs, pushed by Atlantic Water and forced by the gravitational force. Troughs in the shelf edge would introduce another shelf edge profile exemplified in Figure 14. The figure shows that contrary to the standard run there is a raised head leading the gravity current, which is higher than the following flow. This is probably due to the fact that with a continuous shelf edge, water on the shelf experiences an increased gravitational force directed downstream.

Figure 10e shows that the gravity current is better preserved and has a higher density than during the standard run. This gives a higher maximum velocity, Figure 9e, occurring between 4 and 6 km off the shelf edge with a maximum of approximately $0.97\,\mathrm{ms}^{-1}$. Through the whole simulation the gravity current is thicker than during the standard run and as a consequence the gravity current flows further down the shelf slope before reaching a level of equal density.

Figure 8 indicates that oscillations in velocity disappear only when the shelf edge is continous and when non-hydrostatic physics is included. This indicates that the oscillations are a numerical misrepresentation due to the discontinuous shelf edge, and that this can be avoided using non-hydrostatic physics.

5.2.5 Increasing the slope factor

The shelf profile used in these simulations is an idealised shelf profile which represents an average at Ormen Lange. Ormen Lange is located in the core of the Storegga slide that left a headwall at the shelf break of close to 300 km length. Local slope factors may vary throughout the area. Simulations with different slope factor will indicate how this affects the velocities and profile of the gravity currents.

Figure 15 shows that the results are quite similar when we increase the slope factor from 0.03 to 0.04. However, the density distribution differs significantly first 6 hours after simulation start. The head seems to disconnect from the following flow with a steeper slope, and this is confirmed by the density profiles, Figure 10a and f. Also worth noticing is that the fluctuations in the time series of velocity increase with increasing slope factor, Figure 8f.

5.2.6 Decreasing the drag coefficient

The Storegga slide resulted in a particularly rough seabed with large local variations on different scales. This disfavours a constant upper limited drag coefficient and a constant bottom roughness parameter. To investigate the

importance of knowing the correct values, a simulation with zero drag coefficient is performed. We would like to stress that this is not a realistic scenario, but should be considered as a sensitivity test with extreme boundary conditions at the sea floor.

Figure 16 shows that with no drag from the seabed the head of the gravity current collapses. Maximum flow is located at the bottom, as indicated by Figure 9h, and reaches a maximum at about 6 km from the shelf edge of $1.48\,\mathrm{ms}^{-1}$.

With the flow focused close to the seabed, the iso-surfaces of density are quite steep at the level of equal density, about $1027.74\,\mathrm{kgm}^{-3}$.

6 Summary and final remarks

Earlier works have indicated that heavy water may be displaced onto the shelf from large depths. Dense water on the shelf will flow off the shelf and down the shelf slope forced by gravity and held back by friction and entrainment drag until it reaches a level of equal density. Several parameters control the velocity and profile of the flow. Table 3 sums up the results

Simulation	Distances off shelf edge				
	0 km	2 km	4 km	6 km	8km
Standard	0.44	0.85	0.79	0.69	0.60
Vertical resolution	0.44	0.85	0.78	0.73	0.58
Non-hydrostatics	0.91	0.77	0.77	0.71	0.57
Slope factor	0.45	0.90	0.77	0.66	0.24
Initial velocity $U = 0.1\,\mathrm{ms}^{-1}$	0.44	0.84	0.72	0.61	0.38
$U = 0.2\,\mathrm{ms}^{-1}$	0.47	0.82	0.84	0.75	0.62
Drag coefficient	0.47	1.01	1.31	1.48	1.29
Shelf profile	0.65	0.80	0.97	0.97	0.90

Table 3: *Maximum velocity [ms^{-1}] in the water column at stations as indicated in table.*

concerning maximum velocities. The values are highly variable but the prior discussion has indicated that with the present length and vertical scales non-hydrostatics becomes important. With the results from the other sensitivity simulations in mind one can conclude that maximum velocities are almost independent of position down slope, dependant on initial velocity off coast and that one should be careful when addressing the problems of deciding on slope factor, drag coefficient and shelf profile.

The results suggests that with the current initial and boundary conditions maximum velocities are expected to be between 0.7 to 0.8 ms^{-1}.

Acknowledgements

This work has received support from the Research Council of Norway (Programme for Supercomputing) through a grant of computing time. This work has been supported by Norsk Hydro grant NHT-B44-5098606-00.

Appendix A - List of symbols

$\vec{U} = (U, V)$	Horizontal velocities in x- and y-direction respectively
W	Vertical velocity in the z-coordinate system
$\vec{UA} = (U, V)$	Barotropic (depth averaged) velocities in x- and y-direction respectively
ω	Vertical velocity in the σ-coordinate system
η	Surface elevation
H	Bottom Static depth
D	Bottom dynamic depth $(H + \eta)$
P	Pressure
P_{atm}	Atmospheric pressure
T	Temperature
S	Salinity
ρ	In situ density
K_M	Vertical eddy viscosity
A_M	Horizontal eddy viscosity
C_M	Dimensionless horizontal eddy viscosity coefficient
K_H	Vertical eddy diffusivity
A_H	Horizontal eddy diffusivity
C_H	Dimensionless horizontal eddy diffusivity coefficient
$q^2/2$	Turbulent kinetic energy
l	Turbulent macro scale
ρ_0	Reference density
g	Gravity
f	The Coriolis parameter
$\vec{\tau_0} = (\tau_{0x}, \tau_{0y})$	Surface wind stress
$\vec{\tau_b} = (\tau_{bx}, \tau_{by})$	Bottom stress
$\dot{T}_0$	The surface heat flux
$\dot{S}_0$	The net precipitation/evaporation at the surface
$\vec{U_b} = (U_b, V_b)$	Horizontal velocities at the bottom
W_0	Vertical velocity at the surface (z-coordinate)
W_b	Vertical velocity at the bottom (z-coordinate)
C_D	Bottom drag coefficient
κ	The von Karman constant
z_0	Bottom roughness parameter

Appendix B - Figures

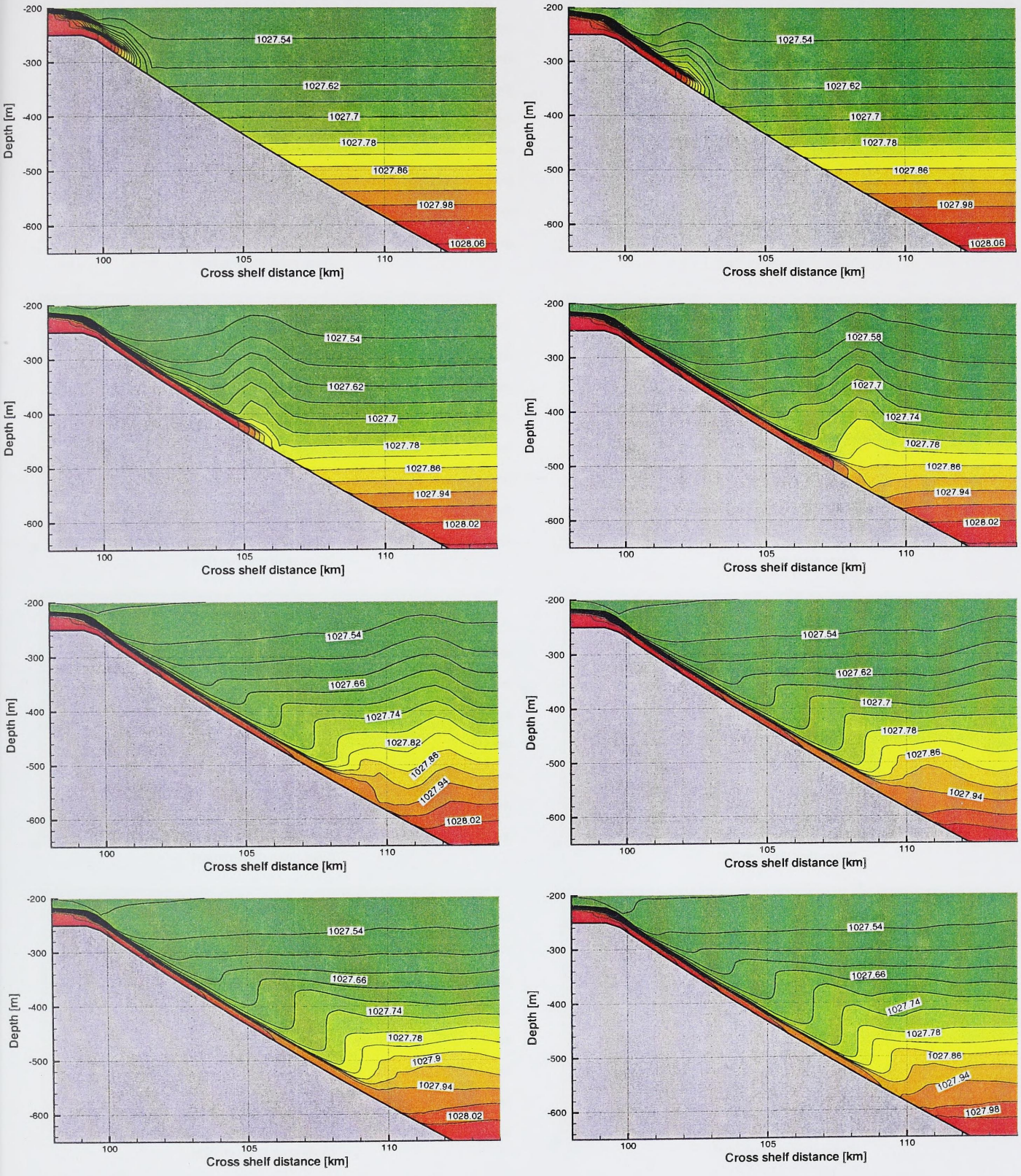

Figure 11: *Vertical section of density 1, 2, 4, 6, 8, 10, 12 and 16 hours after simulation start when increasing the vertical resolution to 70 σ-layers.*

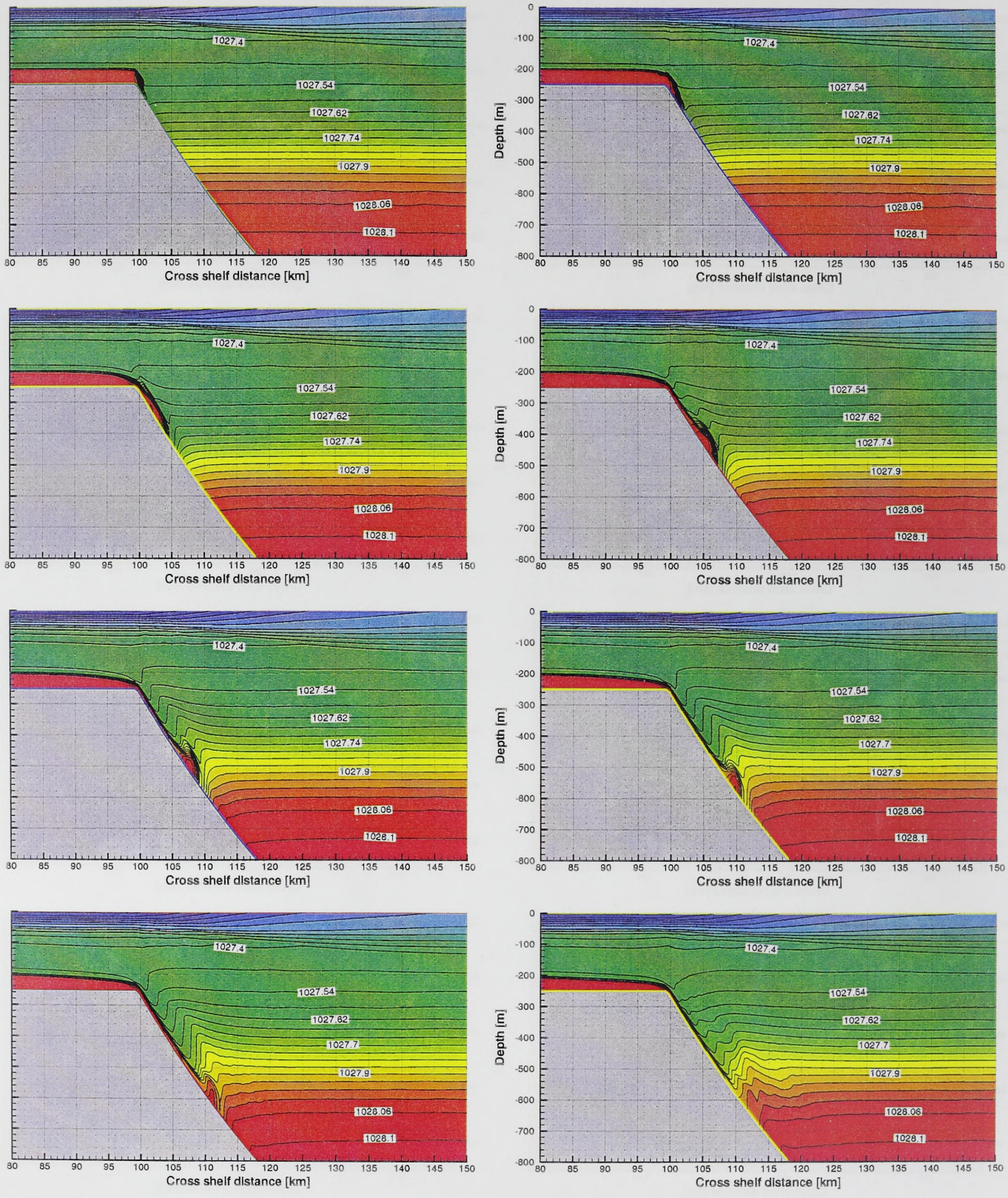

Figure 12: *Vertical section of density 2, 4, 6, 8, 12, 14, 16 and 20 hours after simulation start when including non-hydrostatic physics.*

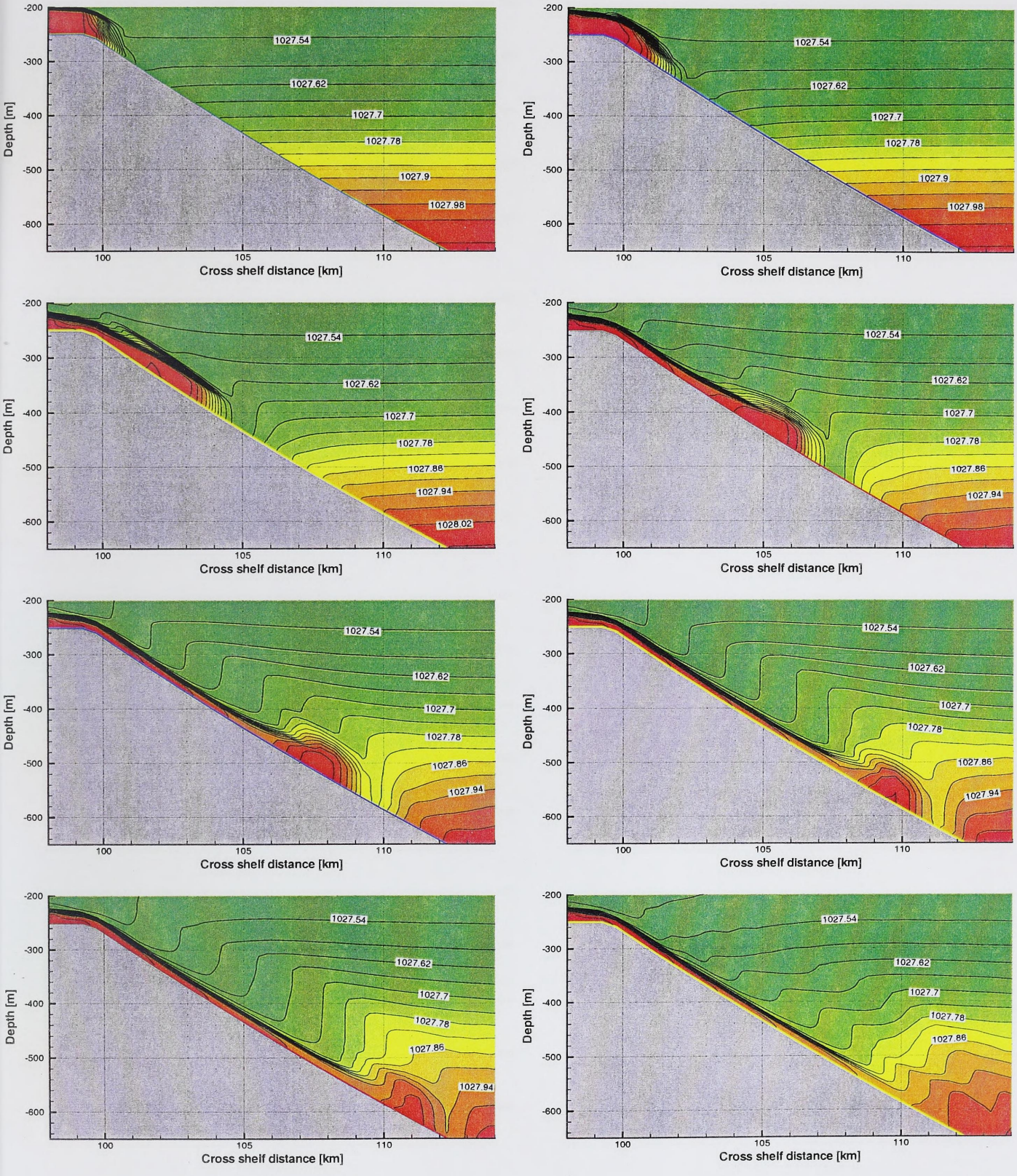

Figure 13: *Vertical section of density 1, 2, 4, 6, 8, 10, 12 and 16 hours after simulation start when including non-hydrostatic physics.*

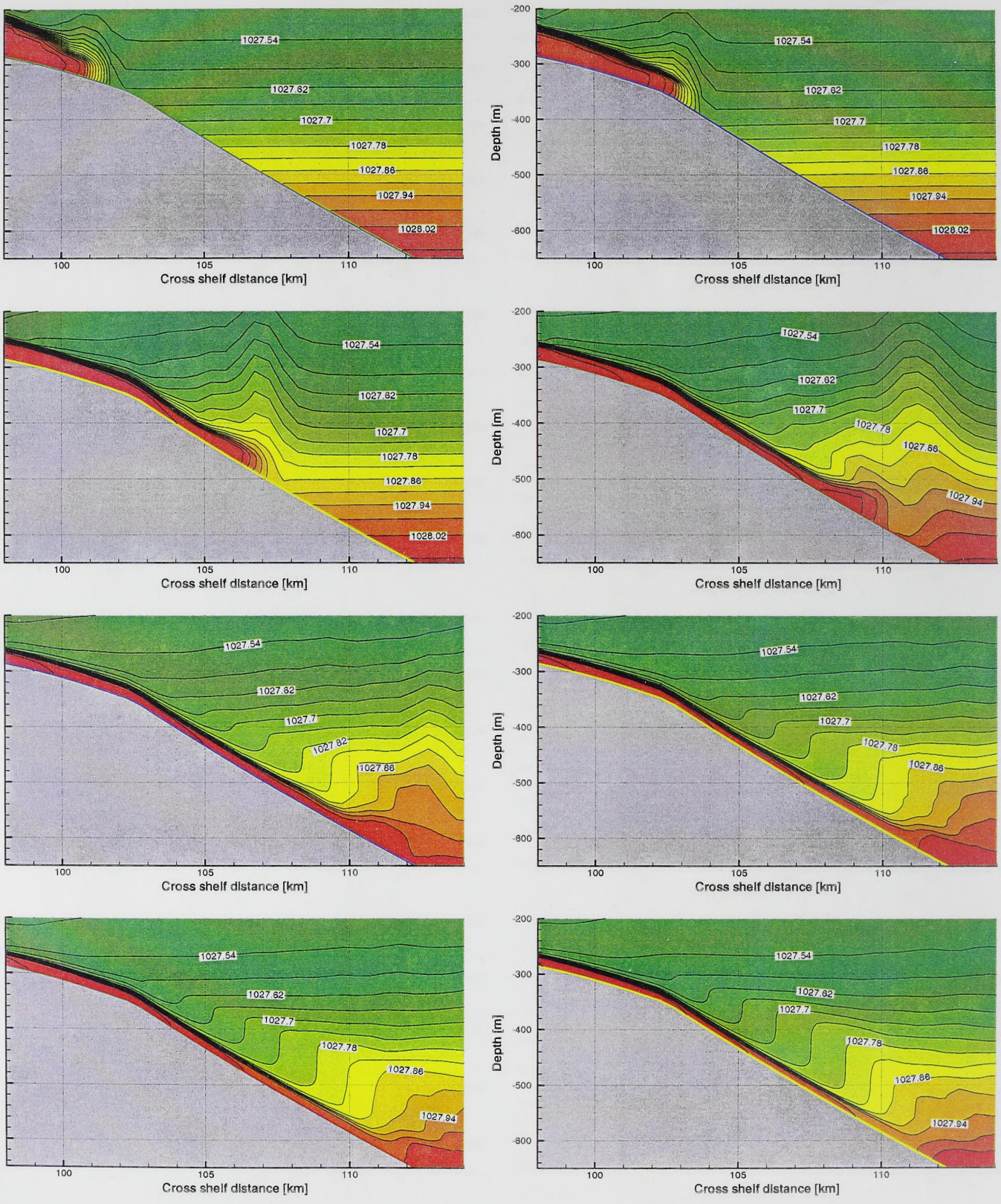

Figure 14: *Vertical section of density 1, 2, 4, 6, 8, 10, 12 and 16 hours after simulation start when introducing a continuous shelf edge.*

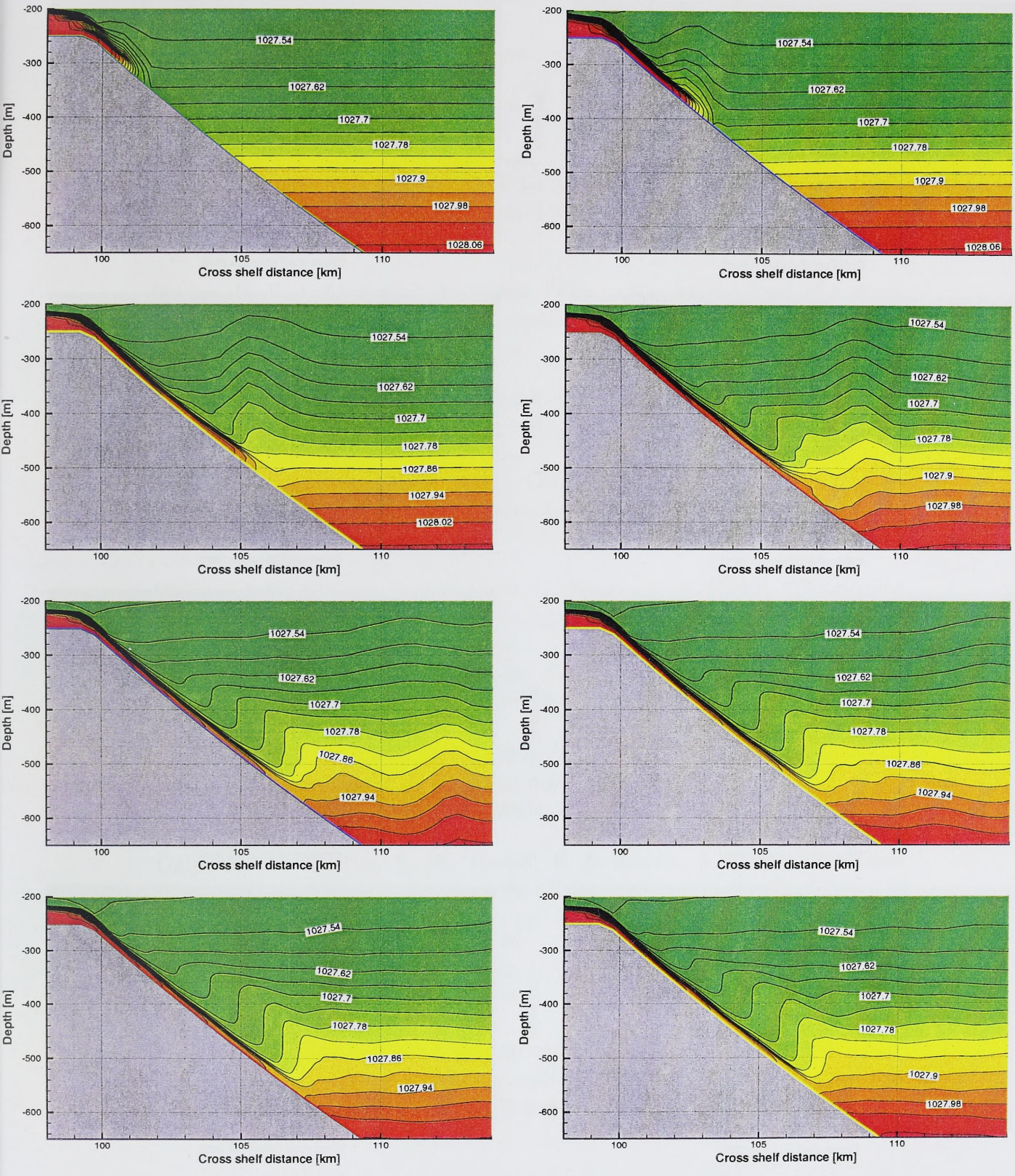

Figure 15: *Vertical section of density 1, 2, 4, 6, 8, 10, 12 and 16 hours after simulation start when increasing the slope factor from 0.03 to 0.04.*

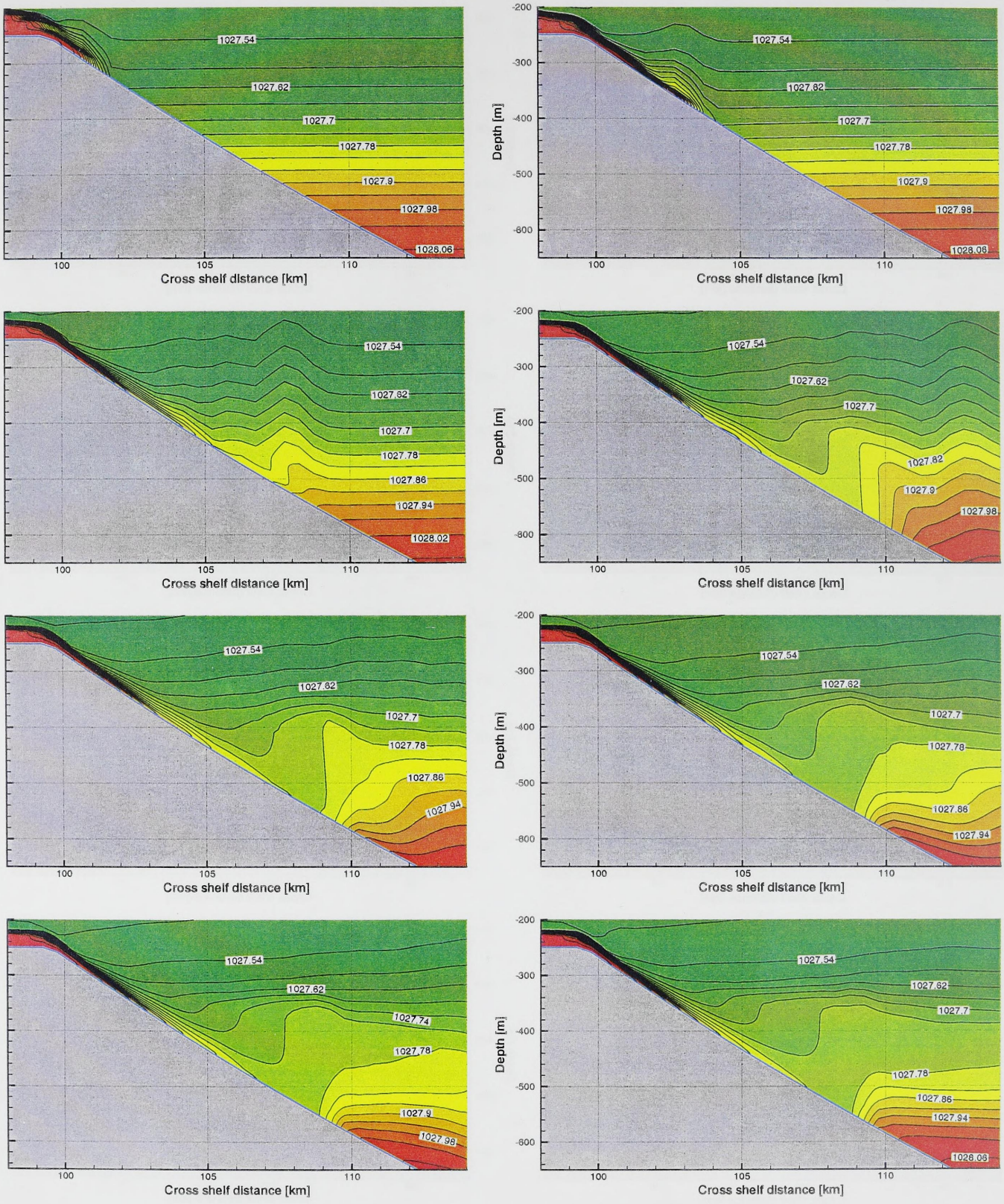

Figure 16: *Vertical section of density 1, 2, 4, 6, 8, 10, 12 and 16 hours after simulation start when setting the drag coefficient equal to zero.*

References

Berntsen, J. (2000), 'USERS GUIDE for a modesplit σ-coordinate numerical ocean model.', *Tech. rep., Dept. of Applied Mathematics, University of Bergen, Vol.135* p. 48.

Britter, R. E. & Linden, P. F. (1980), 'The motion of the front of a gravity current travelling down an incline', *J. Fluid Mech., Vol.99, part 3* pp. 531–543.

Britter, R. E. & Simpson, J. E. (1978), 'Experiments on the dynamics of a gravity current head', *J. Fluid Mech., Vol.88* pp. 223–240.

Eliassen, I. K. & Berntsen, J. (2000), 'Using a sigma-coordinate ocean model for simulating the circulation at ormen lange', *Tech. rep., Dept. of Applied Mathematics, University of Bergen, 138* p. 90.

Eliassen, I. K., Eldevik, T., Berntsen, J. & Furnes, G. K. (2000), 'The current conditions at Ormen Lange - Storegga', p. 22.

Ellison, T. H. & Turner, J. S. (1959), 'Turbulent entrainment in stratified flow', *J. Fluid Mech., Vol.6* pp. 423–448.

Engedahl, H. B. & Røed, L. P. (1999), 'Forecasting ocean currents in deep water areas: the Ormen Lange case', *DNMI Reseach Report No. 80, Norwegian Meteorological Institute* .

Galperin, B., Kantha, L. H., Hassid, S. & Rosati, A. (1988), 'A quasi-equilibrium turbulent energy model for geophysical flows', *Journal of Physical Oceanography, vol.45.* pp. 55–62.

Gill, A. E. (1982), *Atmosphere-Ocean Dynamics*, Academic Press, Inc. ISBN-0-12-283520-4.

Heggelund, Y. & Berntsen, J. (2001), 'Hydrostatic and nonhydrostatic simulations of gravity currents down the shelf slope at Ormen Lange', *Technical Report, Department of Applied Mathematics, University of Bergen, Norway* p. 22.

Martinsen, E. A. & Engedahl, H. (1987), 'Implementation and testing of a lateral boundary scheme as an open boundary condition in a barotropic ocean model', *Coastal Engineering, Vol.11* pp. 603–627.

Mathisen, J. P., Hackett, B. & Engerdahl, H. (2000), 'Description of special current events using observed and simulated data', *OCEANOR report OCN R-99022* .

Mellor, G., Ezer, T. & Oey, L.-Y. (1994), 'The pressure gradient conundrum of sigma coordinate ocean models', *J. Atmos. Oceanic Technol. Vol.11* pp. 1126–1134.

Mellor, G. L. & Blumberg, A. F. (1985), 'Modeling vertical and horizontal diffusivities with the sigms coordinate system', *American Meteorological Society* pp. 1379–1383.

Mellor, G. L. & Yamada, T. (1982), 'Development of a turbulence closure model for geophysical fluid problems', *Reviews of Geophysics and Space Physics, vol.20.* pp. 851–875.

Mesinger, F. & Arakawa, A. (1976), 'Numerical methods used in atmospheric models, Volume I', *WMO/ICSU Joint Organizing Committee, Garp Publication Series No. 17* .

Ommundsen, A. (2000), 'Numeric simulations of tides, shelf slope currents and lagrangian advection of particles', *Phd.Dr.thesis, University of Oslo* .

Simpson, J. E. (1987), *Gravity Currents in the enviroment and the laboratory*, Cambridge University Press. ISBN-0-521-56109-4.

Simpson, J. E. & Britter, R. E. (1979), 'The dynamics of the head of a gravity current advancing over a horizontal surface', *J. Fluid Mech., Vol.94* pp. 477–495.

Smagorinsky, J. (1963), 'General circulation experiments with the primitive equations, I. The basic experiment', *Mon. Weather Rev. Vol 91* pp. 99–164.

Vikebø, F. B., Berntsen, J. & Furnes, G. K. (2001*a*), 'Analysis of measurements at Ormen Lange', *Tech. rep., Dept. of Applied Mathematics, University of Bergen.* .

Vikebø, F. B., Berntsen, J. & Furnes, G. K. (2001*b*), 'Numerical study of the current response at Ormen Lange to a travelling storm', *Tech. rep., Dept. of Applied Mathematics, University of Bergen.* .

Wang, D.-P. (1984), 'Mutual Intrusion of a Gravity Current and Density Front Formation', *J. Phys. Oceanogr. Vol.14* pp. 1191–1199.

Weatherly, G. & Martin, P. J. (1978), 'On the structure and dynamics of the ocean bottom boundary', *J. Phys. Oceanogr.* .